AIAA JOURNAL
Vol. 47, No. 1, January 2009

Laplacian Equivalents to Subsonic Potential Flows

Brian J. German*
Georgia Institute of Technology, Atlanta, Georgia 30332-0150

DOI: 10.2514/1.36877

This paper presents a mapping technique for the solution of Laplacian equivalents to steady subsonic potential flows in the plane. The method employs a coordinate transformation to map a given closed profile and domain in a compressible flow to a related closed profile and domain in a Laplacian flow, with differences in the geometries stemming only from compressibility effects. Unlike certain past methods, the mapping is valid for nonlinear flows with arbitrary density–velocity relations. The theory is implemented in an iterative numerical method in which the Laplacian flow is solved with a boundary element technique, and the compressible flow is then found from a finite difference solution to the mapping. Validation is provided by comparing the resulting subsonic flow solutions to known results in the literature for both a circular cylinder and a NACA 0012 profile. The method is exact in the sense that the inverse mapping of the equivalent Laplacian field recovers the subsonic full-potential solution over the original profile, up to numerical accuracy. Because incompressible potential flows are Laplacian, the mapping yields insights into the phenomenon of compressibility itself in the subsonic setting, and it may have utility in certain aerodynamic test applications.

Nomenclature

a	=	speed of sound
J	=	determinant of the coordinate transformation Jacobian matrix
M	=	Mach number
q	=	velocity magnitude
u	=	x-coordinate velocity in the compressible frame
$\bar{u}$	=	$\bar{x}$-coordinate velocity in the Laplacian frame
v	=	y-coordinate velocity in the compressible frame
$\bar{v}$	=	$\bar{y}$-coordinate velocity in the Laplacian frame
x, y	=	coordinates describing the frame of the given compressible flow
$\bar{x}, \bar{y}$	=	coordinates describing the frame of the equivalent Laplacian flow
α	=	angle of attack in compressible frame
$\bar{\alpha}$	=	angle of attack in Laplacian frame
γ	=	ratio of specific heats
λ	=	ratio of y- to x-component velocities in the compressible frame
ϕ	=	velocity potential
$\tilde{\phi}$	=	perturbation velocity potential
ψ	=	stream function
ρ	=	density
θ	=	flow angle from the x axis in the compressible frame

Subscripts

0	=	stagnation condition
∞	=	freestream condition
$B+$	=	upper domain cut boundary condition
$B-$	=	lower domain cut boundary condition
S	=	inner and outer domain boundary condition
S_I	=	inner domain boundary condition
S_O	=	outer domain boundary condition

Received 28 January 2008; accepted for publication 13 October 2008.

*Assistant Professor, Daniel Guggenheim School of Aerospace Engineering. Member AIAA.

I. Introduction

THE mapping of subsonic flows to related Laplacian flows has been a subject of investigation dating to the early work on the aerodynamic effects of compressibility. The fundamental intent of these mapping approaches has been to transform the compressible potential equation into the Laplace equation in a new coordinate system. In most cases, the boundary conditions and domain resulting from these transformations correspond to a flow that is kinematically identical to an incompressible potential flow over a related profile shape. We term the related flows found through these transformations *Laplacian equivalents* because they directly imply the solution to their corresponding subsonic flows up to the level of approximation of the mappings. The term *incompressible equivalents* may also be proposed, but, for reasons regarding the flow dynamics and transformation of the density, we prefer the former terminology. This reasoning is described in Sec. II.C in the context of the method developed in this paper.

Mappings to equivalent Laplacian flows are of considerable practical and theoretical value. In a practical sense, they allow the vast knowledge base of incompressible potential motion to be carried over directly to the subsonic compressible problem. For instance, the equivalent flows can be solved by any of the myriad of techniques for solutions to the Laplace equation, and the results can be transformed to the frame of the compressible flow to give the results of interest. Similarly, experimental data obtained at low speeds can be transformed to related results at a higher subsonic Mach number. The theoretical value of the mappings lies in the insights that can be gained on the nature of compressibility by understanding the geometric alterations of the domain and immersed bodies necessary to emulate the effect in the incompressible field.

The first efforts in this area were apparently the well-known works of Prandtl [1,2] and Glauert [3] in the potential theory of planar compressible flows. Their approaches, which are substantially similar, map from a flow governed by the subsonic linear potential equation to a Laplacian flow. The method comprises a coordinate scaling, a scaling of the potential function itself to maintain tangency boundary conditions in the related incompressible flow, and an adjustment of the profile slopes independent of the coordinate transformation. The mapping is a global affine transformation that depends on the freestream Mach number.

Scaling the surface slopes independently from the coordinate transformation allows for a variety of similarity rules to be constructed, each manifesting a different relationship between the original and distorted profile shapes as well as between the corresponding pressure coefficients. In the typical implementation, the surface slopes in the equivalent flow are matched to those of the

original compressible flow; therefore, to first order, the coordinate transformation can be neglected, and the effect of the transformation is simply to scale the pressure coefficients. This implementation is the basis of the well-known Prandtl–Glauert rule, which is widely used for compressibility correction of linear potential flows. The adjustment of the profile slopes independent of the coordinate transformation is not strictly correct, but for planar flows, the error is of the order of the linearization. Göthert [4] recognized that for axisymmetric flows, however, the slopes must be adjusted harmoniously with the coordinate transformation to avoid misleading results.

Because they are based on the linearized potential equation, the methods of Prandtl [1,2], Glauert [3], and Göthert [4] provide deteriorating predictive capability as the Mach number of the subsonic flow is increased or as the profile is thickened at a fixed Mach number. The reason for this degradation is that these types of flows are dominated by localized compressibility effects and not the global phenomena corrected by these affine transformations based on the linearized equations of motion.

A type of compressibility correction that includes local compressibility effects was proposed by Chaplygin [5,6]. This method transforms the hodograph equation of a compressible flow into that of an equivalent incompressible flow by introducing a distorted velocity. The method is strictly correct only for flows that obey the linear pressure–volume state relation termed the *tangent gas law*. Chaplygin's method is based on a linearization of the state relation about the stagnation condition, reducing its utility at high subsonic Mach numbers. Tsien [7], acting upon a suggestion by von Kármán, created a similar but substantially improved hodograph method that bases the linearization on the freestream condition. The method involves both a velocity transformation and a profile shape transformation in the physical plane. The approach encounters difficulties for flows with circulation because it transforms a closed airfoil shape into a shape with an open trailing edge.

Although the approach involves a coordinate mapping to redefine the profile shape, this portion of the Kármán–Tsien method is rarely implemented in practical applications. Typically, the magnitude of the profile shape correction is small, and neglecting it has been found to counter the error introduced by the tangent gas approximation [8]. Like the Prandtl–Glauert method, the Kármán–Tsien approach is, therefore, typically implemented as a correction applied to the pressure coefficient obtained from the incompressible flow over the same profile shape as that of the subsonic flow of interest.

In an attempt to resolve the problems with circulatory flows inherent in the Kármán–Tsien approach, Bers [9–11] developed a mapping method to produce an equivalent Laplacian field based in part on concepts from Riemannian geometry. Bers showed that a given compressible flow is related to an equivalent Laplacian flow (which he termed a "conjugate flow") through a conformal mapping in the hodograph plane and a corresponding quasi-conformal mapping in the physical coordinate plane [9,12]. He showed that the mapping could be carried out in closed form for the linear pressure–volume relation of the tangent gas law but that an additional differential equation must be solved for the case of an arbitrary state relation [10,11]. His method is effective for the problem of circulatory flows except that it introduces a singularity that produces a cusp in the profile shape at the leading edge, which causes solution difficulties. Later work by Lin [13,14] solved the problem of circulation by incorporating an intermediate conformal mapping step within the original Kármán–Tsien implementation to ensure trailing-edge closure.

These techniques saw much early success in obtaining approximate subsonic flow solutions, and the Prandtl–Glauert and Kármán–Tsien rules remain relevant in certain contexts for first-order estimates of compressibility effects. By the mid-1950s, however, it was clear that the era of transformation methods for compressible flow solutions was to be surpassed by the era of direct calculation. With the advent of advanced analog and rudimentary digital computers, the possibility of solving nonlinear compressible flows over arbitrary bodies began to emerge. Subsonic potential flow aerodynamic problems can now be solved readily and rapidly by well-established computational techniques.

The shift in emphasis from transformation methods to direct approaches for solving subsonic flows was perhaps a natural one. Whereas transformation methods map to incompressible flows to make solutions tractable, the direct computational approaches obviate the need for the Laplacian intermediate. The direct calculation methods also provide greatly enhanced prediction capability because they require fewer approximations, and, whereas the transformation techniques to equivalent Laplacian flows are valid only for the subsonic case, these direct methods can also solve flows of mixed type.

Although much has been gained in this transition to direct solution methods, there remains an appeal to the notion of equivalent Laplacian flows obtained through a transformation approach. Much of this appeal comes from the original motivation for the classical compressibility corrections, including leveraging the vast knowledge base of incompressible potential motion. The qualitative features of incompressible potential fields are completely understood, and quantitative solutions can be calculated readily by analytical approaches or simple and efficient numerical techniques such as the boundary element method. These flows are also perhaps the best understood in terms of how the external potential field affects viscous phenomena such as boundary layer transition and separation. Additionally, the ability to create Laplcian equivalents may have practical applicability in certain aerodynamic testing scenarios in which the Laplcian flow takes on direct physical meaning as an incompressible flow that can be realized through experiment.

A more fundamental motivation for continuing the investigation of equivalent Laplacian flows is to provide insights into the phenomenon of compressibility itself in the subsonic setting. These insights may be obtained by examining the changes that must be made to a profile shape and coordinate domain in an incompressible flow in order for that flow to mimic a higher Mach subsonic flow. For instance, it is known that the thickness and camber of an airfoil immersed in an incompressible flow must be greater than in a subsonic compressible flow in order to obtain the same pressure coefficient. The ability to quantify these relationships for the fully nonlinear problem may reveal new information about how compressibility effects are equivalent to features of an incompressible domain geometry.

This paper presents a mapping theory to enable the numerical solution of Laplacian equivalents to steady subsonic potential flows in the plane that overcomes certain limitations of earlier methods. Unlike many past methods, the theory is valid for nonlinear circulatory flows with arbitrary density–velocity relations. The theory employs a coordinate transformation to map a given domain and closed profile in a compressible flow to a related domain and closed profile in a Laplacian flow. The method is a pure coordinate mapping in the physical plane; that is, transformations such as the scaling of the potential field or the definition of a distorted velocity in the hodograph plane are not required. Boundary conditions for the mapping are chosen such that differences in the profile shapes stem only from the effects of compressibility; the transformation does not map an arbitrary airfoil into a circle as in certain past methods. The approach is exact in the sense that the inverse mapping of the equivalent Laplacian field recovers the subsonic full-potential solution over the original profile, up to numerical accuracy.

II. Mapping Theory

A. Governing Equations

For compressible potential flow in the plane, the governing equations of steady motion can be written in Cartesian coordinates as

$$\frac{\partial \psi}{\partial y} = \rho \frac{\partial \phi}{\partial x} \qquad -\frac{\partial \psi}{\partial x} = \rho \frac{\partial \phi}{\partial y} \tag{1}$$

The density ρ is obtained from the potential as

$$\rho = \rho_0 \left\{ 1 - \frac{(\gamma - 1)}{2a_0^2} \left[\left(\frac{\partial \phi}{\partial x} \right)^2 + \left(\frac{\partial \phi}{\partial y} \right)^2 \right] \right\}^{1/(\gamma - 1)} \tag{2}$$

in which ρ_0 and a_0 are stagnation values of the density and sound speed, respectively. Equation (1) is equivalent to the continuity and irrotationality conditions as can be verified by cross differentiating and equating the resulting mixed second partial derivatives.

The objective is to map a given compressible flow of arbitrary γ governed by Eqs. (1) and (2) into a flow governed by

$$\frac{\partial \psi}{\partial \bar{y}} = \rho_0 \frac{\partial \phi}{\partial \bar{x}} \qquad -\frac{\partial \psi}{\partial \bar{x}} = \rho_0 \frac{\partial \phi}{\partial \bar{y}} \tag{3}$$

through the transformation of coordinates

$$\bar{x} = \bar{x}(x, y) \qquad \bar{y} = \bar{y}(x, y) \tag{4}$$

Equation (3) shows the Cauchy–Riemann equations of complex analysis, which indicate that the flow is Laplacian.

Although any constant density could be selected in place of ρ_0 to produce a Laplacian flow, the stagnation value is chosen because a compressible flow transitions naturally to an incompressible flow in stagnation regions. Through this choice, the coordinate transformation in the local neighborhood of a stagnation point will be shown to relax to the identity transformation. The profile shape will, therefore, be as smooth in the stagnation regions as the original shape in the domain of the compressible flow, and certain difficulties associated with singularities in the transformed shape that are encountered with the method of Bers [10,11] are avoided.

To pose the coordinate mapping problem, we begin by applying the chain rule to the partial derivatives that appear in Eq. (3) to transform them to the (x, y) frame:

$$\begin{aligned} \left[\frac{\partial \psi}{\partial x}\frac{\partial x}{\partial \bar{y}} + \frac{\partial \psi}{\partial y}\frac{\partial y}{\partial \bar{y}} \right] &= \rho_0 \left[\frac{\partial \phi}{\partial x}\frac{\partial x}{\partial \bar{x}} + \frac{\partial \phi}{\partial y}\frac{\partial y}{\partial \bar{x}} \right] \\ -\left[\frac{\partial \psi}{\partial x}\frac{\partial x}{\partial \bar{x}} + \frac{\partial \psi}{\partial y}\frac{\partial y}{\partial \bar{x}} \right] &= \rho_0 \left[\frac{\partial \phi}{\partial x}\frac{\partial x}{\partial \bar{y}} + \frac{\partial \phi}{\partial y}\frac{\partial y}{\partial \bar{y}} \right] \end{aligned} \tag{5}$$

We shall find it more useful to express all partial derivatives in terms of the (x, y) frame. Toward this end, we can write the coordinate derivatives in terms of their inverses as

$$\frac{\partial x}{\partial \bar{x}} = \frac{1}{J}\frac{\partial \bar{y}}{\partial y}, \qquad \frac{\partial x}{\partial \bar{y}} = -\frac{1}{J}\frac{\partial \bar{x}}{\partial y} \qquad \frac{\partial y}{\partial \bar{x}} = -\frac{1}{J}\frac{\partial \bar{y}}{\partial x}, \qquad \frac{\partial y}{\partial \bar{y}} = \frac{1}{J}\frac{\partial \bar{x}}{\partial x} \tag{6}$$

where

$$J = \left| \frac{\partial(\bar{x}, \bar{y})}{\partial(x, y)} \right|$$

is the determinant of the Jacobian matrix. Using these relations in Eq. (5) results in

$$\begin{aligned} \left[-\frac{\partial \psi}{\partial x}\frac{\partial \bar{x}}{\partial y} + \frac{\partial \psi}{\partial y}\frac{\partial \bar{x}}{\partial x} \right] &= \rho_0 \left[\frac{\partial \phi}{\partial x}\frac{\partial \bar{y}}{\partial y} - \frac{\partial \phi}{\partial y}\frac{\partial \bar{y}}{\partial x} \right] \\ -\left[\frac{\partial \psi}{\partial x}\frac{\partial \bar{y}}{\partial y} - \frac{\partial \psi}{\partial y}\frac{\partial \bar{y}}{\partial x} \right] &= \rho_0 \left[-\frac{\partial \phi}{\partial x}\frac{\partial \bar{x}}{\partial y} + \frac{\partial \phi}{\partial y}\frac{\partial \bar{x}}{\partial x} \right] \end{aligned} \tag{7}$$

Employing Eq. (1) to replace ψ derivatives with ϕ derivatives, Eq. (7) becomes

$$\begin{aligned} \rho \left[\frac{\partial \phi}{\partial y}\frac{\partial \bar{x}}{\partial y} + \frac{\partial \phi}{\partial x}\frac{\partial \bar{x}}{\partial x} \right] &= \rho_0 \left[\frac{\partial \phi}{\partial x}\frac{\partial \bar{y}}{\partial y} - \frac{\partial \phi}{\partial y}\frac{\partial \bar{y}}{\partial x} \right] \\ \rho \left[\frac{\partial \phi}{\partial y}\frac{\partial \bar{y}}{\partial y} + \frac{\partial \phi}{\partial x}\frac{\partial \bar{y}}{\partial x} \right] &= \rho_0 \left[-\frac{\partial \phi}{\partial x}\frac{\partial \bar{x}}{\partial y} + \frac{\partial \phi}{\partial y}\frac{\partial \bar{x}}{\partial x} \right] \end{aligned} \tag{8}$$

Solving Eq. (8) for the $\bar{x}$ derivatives gives

$$\begin{aligned} \frac{\partial \bar{x}}{\partial x} &= \lambda \left[\frac{(\rho/\rho_0) - (\rho_0/\rho)}{1 + \lambda^2} \right] \frac{\partial \bar{y}}{\partial x} + \left[\frac{(\rho/\rho_0)\lambda^2 + (\rho_0/\rho)}{1 + \lambda^2} \right] \frac{\partial \bar{y}}{\partial y} \\ \frac{\partial \bar{x}}{\partial y} &= -\left[\frac{(\rho/\rho_0) + (\rho_0/\rho)\lambda^2}{1 + \lambda^2} \right] \frac{\partial \bar{y}}{\partial x} - \lambda \left[\frac{(\rho/\rho_0) - (\rho_0/\rho)}{1 + \lambda^2} \right] \frac{\partial \bar{y}}{\partial y} \end{aligned} \tag{9}$$

where $\lambda = (\frac{\partial \phi}{\partial y})/(\frac{\partial \phi}{\partial x}) = \tan\theta$, and θ is the flow angle relative to the x axis in the original Cartesian frame of the compressible flow. Similarly, solving instead for the $\bar{y}$ derivatives results in

$$\begin{aligned} \frac{\partial \bar{y}}{\partial x} &= -\lambda \left[\frac{(\rho/\rho_0) - (\rho_0/\rho)}{1 + \lambda^2} \right] \frac{\partial \bar{x}}{\partial x} - \left[\frac{(\rho/\rho_0)\lambda^2 + (\rho_0/\rho)}{1 + \lambda^2} \right] \frac{\partial \bar{x}}{\partial y} \\ \frac{\partial \bar{y}}{\partial y} &= \left[\frac{(\rho/\rho_0) + (\rho_0/\rho)\lambda^2}{1 + \lambda^2} \right] \frac{\partial \bar{x}}{\partial x} + \lambda \left[\frac{(\rho/\rho_0) - (\rho_0/\rho)}{1 + \lambda^2} \right] \frac{\partial \bar{x}}{\partial y} \end{aligned} \tag{10}$$

Equations (9) and (10) are Beltrami differential equations for the coordinates $\bar{x}$ and $\bar{y}$, respectively. These equations are generalizations of the Cauchy–Riemann equations. Whereas the Cauchy–Riemann equations govern conformal transformations, the Beltrami equations govern mappings that are termed quasi conformal [12].

Equation (9) or equivalently Eq. (10) provides two equations for the four unknown partial derivatives of the coordinate transformation. The remaining two relations cannot be specified arbitrarily throughout the domain, as the integrability conditions for the coordinate transformation must also be satisfied, that is, the mixed second partial derivatives must commute in order that $\bar{x}$ and $\bar{y}$ have unique values at any particular point). It is for this reason that the Beltrami equations are to be interpreted as differential equations.

To enforce the integrability conditions, we take the y derivative of the first equation in each pair and equate the resulting expression to the x derivative of the corresponding second equation. This process results in

$$\begin{aligned} &\frac{\partial}{\partial y}\left\{ \lambda \left[\frac{(\rho/\rho_0) - (\rho_0/\rho)}{1 + \lambda^2} \right] \frac{\partial \bar{y}}{\partial x} + \left[\frac{(\rho/\rho_0)\lambda^2 + (\rho_0/\rho)}{1 + \lambda^2} \right] \frac{\partial \bar{y}}{\partial y} \right\} \\ &\quad + \frac{\partial}{\partial x}\left\{ \left[\frac{(\rho/\rho_0) + (\rho_0/\rho)\lambda^2}{1 + \lambda^2} \right] \frac{\partial \bar{y}}{\partial x} + \lambda \left[\frac{(\rho/\rho_0) - (\rho_0/\rho)}{1 + \lambda^2} \right] \frac{\partial \bar{y}}{\partial y} \right\} \\ &\quad = 0 \end{aligned} \tag{11}$$

and

$$\begin{aligned} &\frac{\partial}{\partial y}\left\{ \lambda \left[\frac{(\rho/\rho_0) - (\rho_0/\rho)}{1 + \lambda^2} \right] \frac{\partial \bar{x}}{\partial x} + \left[\frac{(\rho/\rho_0)\lambda^2 + (\rho_0/\rho)}{1 + \lambda^2} \right] \frac{\partial \bar{x}}{\partial y} \right\} \\ &\quad + \frac{\partial}{\partial x}\left\{ \left[\frac{(\rho/\rho_0) + (\rho_0/\rho)\lambda^2}{1 + \lambda^2} \right] \frac{\partial \bar{x}}{\partial x} + \lambda \left[\frac{(\rho/\rho_0) - (\rho_0/\rho)}{1 + \lambda^2} \right] \frac{\partial \bar{x}}{\partial y} \right\} \\ &\quad = 0 \end{aligned} \tag{12}$$

which are second-order partial differential equations for the coordinate mapping.

Owing to the presence of the variable density ρ and the flow angle expression λ in Eqs. (11) and (12), the mapping is a function of the flow. For a given flow solution, the mapping is obtained by solving both equations with specified boundary conditions. Boundary conditions given in terms of one of the mapped coordinates, say $\bar{x}$, imply corresponding conditions on the other coordinate $\bar{y}$ through the Beltrami equations. As shown in the Appendix, these mapping equations are elliptic regardless of the particular flow solution, and they, therefore, require that conditions be given on all domain boundaries. The boundary value problem for the mapping is described in Sec. II.B.

The mapping can be determined a posteriori for a given flow solution, or, alternately, it can be solved simultaneously with the flow. In a simultaneous solution, estimates for the equivalent flow in the $(\bar{x}, \bar{y})$ system can be found using a boundary element technique such as a panel method because the flow obeys the Laplace equation in that frame. These estimates can be used to generate the values ρ and λ needed to produce estimates for the mapping. This process of solving first the equivalent Laplacian flow and then the coordinate

mapping can be iterated to convergence. An implementation of this iterative approach is outlined in Sec. III to produce the results presented in Sec. IV.

B. Boundary Value Problem for the Coordinate Mapping

We consider the two-dimensional boundary value problem for an isolated airfoil in free flow. The domain topology is shown in Fig. 1, in which the interior is denoted as V, the boundary curve is termed S, and the airfoil chord is oriented in the x direction. The boundary S comprises the interior boundary S_I describing the immersed airfoil and the outer far-field boundary S_O, that is, $S = S_I \cup S_O$). The far-field boundary is envisioned to extend to infinity, or at least to the point that the equations governing the flow can be linearized. The cut barriers B_+ and B_- are inserted into the domain to transform the doubly connected region exterior to the airfoil into a simply connected region. Thinking of the domain as a typical o-grid topology, the cut barriers serve the roles of the remaining two sides of the computational rectangle upon which the domain is typically mapped.

We are interested in choosing boundary conditions that transform a smooth airfoil shape with a closed trailing edge into a second smooth and closed airfoil shape of the same chord with distortions owing only to the effects of compressibility. More specifically, we require the mapping to reduce to the identity transformation in the limit of $\rho \to \rho_0$ globally, that is, as the compressible flow transitions to an incompressible flow. The advantage of this approach is that a given airfoil shape and domain in compressible flow is mapped to an airfoil shape and domain in incompressible flow with substantially similar geometry. This approach is in the same spirit as the original Prandtl–Glauert similarity transformations for linearized flows.

Toward this end, we specify the Dirichlet conditions

$$\bar{x}|_S = x|_S \tag{13}$$

to match the abscissa coordinate along the entire domain boundary. These conditions therefore imply chord preservation along the airfoil. To close the problem, we also specify periodic boundary conditions on the cut barriers in the form

$$\bar{y}|_{B_+} = \bar{y}|_{B_-} \tag{14}$$

to prevent the trailing edge from opening. This statement is equivalent to the requirement that $\bar{y}$ be single valued along the cut, and in this sense, it is the analog of the specification of vanishing circulation in the determination of the potential.

We can verify that this transformation reduces to the identity transformation in the incompressible limit and in stagnation regions as follows. In the limit $\rho \to \rho_0$, Eq. (9) reduces to the Cauchy–Riemann equations and Eqs. (11) and (12) become Cartesian Laplace equations for $\bar{y}$ and $\bar{x}$, respectively. The Laplace equation for $\bar{x}$ and the Dirichlet boundary conditions in Eq. (13) are satisfied by the solution $\bar{x}|_{S\cup V} = x|_{S\cup V}$, and it is a well-known result that the Dirichlet problem for the Laplace equation is unique. Considering this solution, the Cauchy–Riemann equations imply that the unique solution for $\bar{y}$ is given by $\bar{y}|_{S\cup V} = y|_{S\cup V}$. This unique mapping is, therefore, the identity mapping.

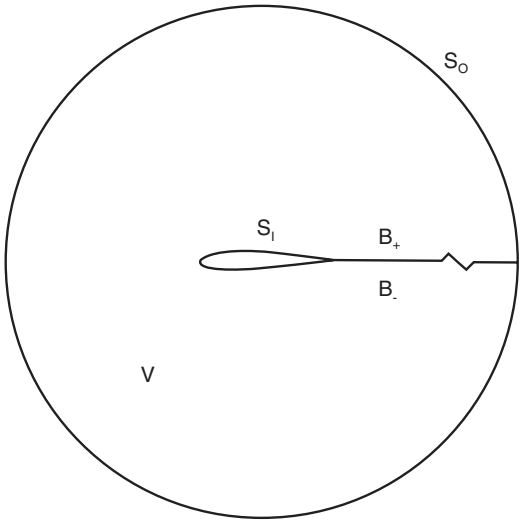

Fig. 1 Domain layout for an isolated airfoil.

C. Transformation of the Flow Properties and Boundary Conditions

We now investigate the effects of this coordinate transformation on the flow field. In particular, we are interested in the transformation of the scalar and vector properties and the boundary value problem of the flow. This information is important for understanding the physical nature of the equivalent Laplacian flow as well in transferring information from the compressible to the equivalent Laplacian domain and vice versa.

We first describe the transformation of flow properties between the two coordinate systems. Scalar properties do not depend on the choice of coordinates and are therefore invariants of the transformation. That is, the scalar values are the same at a corresponding point τ in both systems even though the point will, in general, be individuated by different coordinate values, namely $(x|_\tau, y|_\tau)$ in the original frame and $(\bar{x}|_\tau, \bar{y}|_\tau)$ in the frame of the equivalent Laplacian flow. This transformation behavior indicates that even in the equivalent Laplacian flow of the $(\bar{x}, \bar{y})$ system, the thermodynamic density actually varies from point to point in the same way as for the original subsonic compressible flow in the (x, y) system.

This variation implies that it is appropriate to think of the thermodynamic scalar properties as being physically defined in the original (x, y) frame of the original compressible flow. The thermodynamic quantities can be determined from a known kinematic solution in this frame through expressions such as the density–velocity relation given by Eq. (2); therefore, they can also be determined from a known kinematic solution in the $(\bar{x}, \bar{y})$ frame of the equivalent flow by consideration of the velocity transformation behavior. This behavior is dictated by the transformation law for covariant vectors, which implies interrelationships of the form

$$\frac{\partial \phi}{\partial x} = \frac{\partial \phi}{\partial \bar{x}}\frac{\partial \bar{x}}{\partial x} + \frac{\partial \phi}{\partial \bar{y}}\frac{\partial \bar{y}}{\partial x} \Leftrightarrow \frac{\partial \phi}{\partial \bar{x}} = \frac{\partial \phi}{\partial x}\frac{\partial x}{\partial \bar{x}} + \frac{\partial \phi}{\partial y}\frac{\partial y}{\partial \bar{x}} \tag{15}$$

for example. Other covariant vectors such as the mass flux obey similar transformation laws. A key implication of this behavior is that the pressure coefficient must be calculated using the compressible flow relation in the original frame and not using the incompressible relation in the Laplacian frame. The variation of the thermodynamic scalar properties is the motivation for our preference of the term equivalent Laplacian flows instead of equivalent incompressible flows. Although this qualification is important, it will be shown that the equivalent Laplacian flow can be interpreted as a realistic incompressible potential flow over a body. The only caveat in this interpretation is that we must transform velocities to calculate pressure coefficients and other scalar dynamic properties for the corresponding subsonic flow.

We now consider the transformation of the boundary value problem for the flow. In particular, we are interested in the boundary conditions along the inner and outer domain borders, the angle of attack, and the Kutta condition.

For the typical external aerodynamic problem, the condition at the inner boundary S_I is flow tangency to the immersed profile. This condition requires that the velocity component normal to the airfoil vanish, which amounts to the requirement that the scalar product of the velocity vector and the surface normal vector equate to zero. A scalar product is coordinate invariant, and so the statement of flow tangency to the boundary curve is independent of the particular coordinate parametrization. The flow must therefore be tangent to the airfoil drawn in $(\bar{x}, \bar{y})$ as well as the to the airfoil drawn in the (x, y) frame. This behavior reflects the physical nature of the requirement of flow tangency.

To examine the transformation of the outer boundary conditions and the angle of attack, we first consider the limiting form of the governing flow equations in the far field for both coordinate systems. For the compressible potential flow in the original Cartesian coordinates (x, y), this limiting form is the linearized planar potential equation

$$\left(1-\frac{u_\infty^2}{a_\infty^2}\right)\frac{\partial^2\phi}{\partial x^2}-\frac{2u_\infty v_\infty}{a_\infty^2}\frac{\partial^2\phi}{\partial x\partial y}+\left(1-\frac{v_\infty^2}{a_\infty^2}\right)\frac{\partial^2\phi}{\partial y^2}=0 \qquad (16)$$

which is the well known Prandtl–Glauert equation written for an arbitrarily aligned freestream. The quantities u_∞ and v_∞ are the x and y components of the freestream velocity, respectively, and a_∞ is the freestream sound speed. In the frame $(\bar{x}, \bar{y})$ of the equivalent flow, the governing equation takes the same form in the far-field limit as in the domain interior, namely, the Cartesian Laplace equation

$$\frac{\partial^2\phi}{\partial\bar{x}^2}+\frac{\partial^2\phi}{\partial\bar{y}^2}=0 \qquad (17)$$

To determine the transformation of the angle of attack and the far-field boundary conditions, we must determine the implications of these limiting flow equations on the freestream limit of the coordinate mapping. Because the Prandtl–Glauert equation governs the subsonic flow at an infinite distance from the airfoil and the transformation maps to the Laplace equation, the mapping in this neighborhood should resemble a form of the Prandtl–Glauert transformation. In particular, the first derivatives of the transformation should be constants such that the mapping is a uniform stretching or shrinking in the far field. This transformation must also obey the Dirichlet condition specified by Eq. (13) along the far-field boundary. The unique transformation that meets these requirements is

$$\begin{aligned}\bar{x}|_{S_o} &= x|_{S_o}\\ \bar{y}|_{S_o} &= \frac{1}{\sqrt{1-M_\infty^2}}[(u_\infty v_\infty/a_\infty^2)x|_{S_o}+(1-u_\infty^2/a_\infty^2)y|_{S_o}]\end{aligned} \qquad (18)$$

which has

$$\begin{aligned}\left.\frac{\partial\bar{x}}{\partial x}\right|_{S_o} &= 1 \qquad \left.\frac{\partial\bar{x}}{\partial y}\right|_{S_o}=0\\ \left.\frac{\partial\bar{y}}{\partial x}\right|_{S_o} &= \frac{u_\infty v_\infty/a_\infty^2}{\sqrt{1-M_\infty^2}} \qquad \left.\frac{\partial\bar{y}}{\partial y}\right|_{S_o}=\frac{(1-u_\infty^2/a_\infty^2)}{\sqrt{1-M_\infty^2}}\end{aligned} \qquad (19)$$

as the constant first transformation derivatives in the far field and

$$\begin{aligned}\left.\frac{\partial x}{\partial\bar{x}}\right|_{S_o} &= 1 \qquad \left.\frac{\partial x}{\partial\bar{y}}\right|_{S_o}=0\\ \left.\frac{\partial y}{\partial\bar{x}}\right|_{S_o} &= -\frac{u_\infty v_\infty/a_\infty^2}{(1-u_\infty^2/a_\infty^2)} \qquad \left.\frac{\partial y}{\partial\bar{y}}\right|_{S_o}=\frac{\sqrt{1-M_\infty^2}}{(1-u_\infty^2/a_\infty^2)}\end{aligned} \qquad (20)$$

as their inverses.

The transformation of the angle of attack α can now be determined. In the original Cartesian frame of the subsonic flow, the angle is defined as

$$\tan\alpha=\frac{v_\infty}{u_\infty} \qquad (21)$$

The freestream velocity components in the original frame can now be related to those in the Laplacian equivalent frame using the transformation law for covariant vectors as

$$\bar{u}_\infty=u_\infty\frac{\partial x}{\partial\bar{x}}+v_\infty\frac{\partial y}{\partial\bar{x}} \qquad \bar{v}_\infty=u_\infty\frac{\partial x}{\partial\bar{y}}+v_\infty\frac{\partial y}{\partial\bar{y}}$$

Substituting Eq. (19) and simplifying results in

$$\bar{u}_\infty=\frac{(1-M_\infty^2)u_\infty}{(1-u_\infty^2/a_\infty^2)} \qquad \bar{v}_\infty=\frac{(\sqrt{1-M_\infty^2})v_\infty}{(1-u_\infty^2/a_\infty^2)} \qquad (22)$$

Employing Eq. (22) in Eq. (21) gives,

$$\tan\alpha=\frac{(1-M_\infty^2)}{\sqrt{1-M_\infty^2}}\frac{\bar{v}_\infty}{\bar{u}_\infty}=\sqrt{1-M_\infty^2}\frac{\bar{v}_\infty}{\bar{u}_\infty} \qquad (23)$$

If we now identify $\bar{\alpha}$ as the angle of attack defined by treating $(\bar{x}, \bar{y})$ as a Cartesian system, then

$$\tan\bar{\alpha}=\frac{\bar{v}_\infty}{\bar{u}_\infty} \qquad (24)$$

and Eq. (23) becomes

$$\tan\alpha=\sqrt{1-M_\infty^2}\tan\bar{\alpha} \qquad (25)$$

or

$$\tan\bar{\alpha}=\frac{1}{\sqrt{1-M_\infty^2}}\tan\alpha \qquad (26)$$

Equation (26) is the transformation of the angle of attack that we seek. It indicates that the tangent of the angle of attack in the canonical Laplacian flow is larger than that of the subsonic flow by a factor identical to that obtained in certain forms of the Prandtl–Glauert rule. This result is reassuring because we have predicated this transformation on the fact that the subsonic flow can be treated as a linear compressible flow in the far-field region.

The far-field boundary condition for subsonic full-potential external flow is specified as a function of the circulation around the airfoil in the form

$$\hat{\phi}=\frac{\Gamma}{2\pi}\tan^{-1}\left[\sqrt{1-M_\infty^2}\left(\frac{yu_\infty-xv_\infty}{xu_\infty+yv_\infty}\right)\right] \qquad (27)$$

where $\hat{\phi}=\phi-\phi_\infty$ is the perturbation potential and x and y are the signed coordinate distances in the original frame from any particular boundary point to a discrete vortex with strength Γ located along the airfoil chord line. In the case of nonlifting flows without circulation, Γ vanishes, and the condition reduces to $\hat{\phi}=0$ along the far-field boundary. Equation (27) can be shown to satisfy Eq. (16).

Applying the far-field coordinate transformation of Eq. (18), Eq. (27) becomes

$$\hat{\phi}=\frac{\Gamma}{2\pi}\tan^{-1}\left(\frac{\bar{y}\bar{u}_\infty-\bar{x}\bar{v}_\infty}{\bar{x}\bar{u}_\infty+\bar{y}\bar{v}_\infty}\right) \qquad (28)$$

which can be recognized as the far-field influence of a discrete vortex in incompressible flow that satisfies the Laplace Eq. (17) when the $(\bar{x}, \bar{y})$ frame is viewed as a Cartesian system.

The last goal in this section is to establish the transformation behavior of the Kutta condition for lifting flows. The Kutta condition prescribes that the flow should leave the airfoil trailing edge smoothly, and for airfoils with a finite trailing-edge angle, the trailing edge must be a stagnation point [15]. The condition must be enforced in order to prescribe the circulation for lifting flows around airfoils in both incompressible and subsonic compressible flows.

One interpretation of the Kutta condition is that the velocities along the upper and lower surfaces of an airfoil must approach the same value at the trailing edge. Because the tangency boundary condition is preserved in the coordinate transformation, the flow is tangent both to the original airfoil surface and to the airfoil surface in the transformed frame. Because the Kutta condition can be described in terms of velocities tangent to the trailing-edge surfaces, it must be expressed in the same way in the equivalent Laplacian flow as in the original flow.

In summary, the equivalent flow is kinematically identical to an incompressible flow in the frame $(\bar{x}, \bar{y})$ with tangency boundary conditions and the expected far-field circulatory behavior when we

consider these coordinates as a Cartesian system. This result implies that the equivalent flow can be solved in this frame by any standard incompressible aerodynamic solution technique, and the flow approximates a true incompressible flow over a solid body in free flow.

III. Numerical Method

A direct approach to determining an equivalent Laplacian flow is to solve Eqs. (11) and (12) subject to the boundary condition in Eqs. (13) and (14) for a known subsonic potential flow solution. The known subsonic solution provides the required values of ρ and λ that distort the coordinates of the original flow problem into those of the Laplacian equivalent. These subsonic potential solutions can be obtained by a numerical full-potential solution technique, or, if viscous and three-dimensional effects are negligible, experimental subsonic solutions could be used. Once the full-potential solution is known, the coordinate mapping can be found in a single application of an elliptic boundary value solver.

An alternative, indirect approach is employed to generate the results presented in this paper. This approach consists of an iterative solution obtained by repeatedly calculating estimates for the equivalent Laplacian flow and then the coordinate mapping, with each new mapping improving the subsequent estimate of the equivalent domain and flow solution. The general solution algorithm is shown in Fig. 2. The equivalent flow is solved with a boundary element panel method, and corresponding estimates for the subsonic flow over the original geometry are generated through the coordinate mapping solution.

This approach is implemented in a nested-loop structure, with the inner loop consisting of the iterative coordinate mapping algorithm that is converged for each iteration of the outer loop corresponding to a new flow solution. It should be noted that this method is expected to be less computationally efficient than the direct approach because of its doubly iterative nature; however, because the panel method is correct only for Laplacian flows, developing the solution in this way offers an additional technique for gauging the validity of the theory, that is, we solve the subsonic flow through its Laplacian equivalent and can compare to results in the literature). This approach is also in the spirit of the original compressibility correction techniques that acted as operators on the Laplacian flow solution. This section outlines the general approach of this iterative method, and details of the implementation are given in a previous work by the author [16].

The first step in this indirect solution method is to develop a domain grid corresponding to the geometry of the given subsonic compressible flow. For this work, a structured o-grid topology is employed. Detailed grid sensitivity studies of the node density and the location of the freestream boundary for the method are presented in German [16]. The results of these studies for nonlifting flow over a circular cylinder at $M_\infty = 0.375$ indicate that grid independence is attained for all practical purposes with a uniform algebraically defined 121×121 linear node distribution in the circumferential and radial directions and a outer-to-inner boundary radius ratio of $R_O/R_I = 6$. These settings were used to produce the flow solutions described subsequently in Sec. IV.A of this paper. The values of these grid parameters must, in general, be examined for each domain geometry and freestream Mach number. At higher subsonic Mach numbers, the freestream boundary must be moved outward relative to the profile thickness because of the persistence of flow disturbances to a greater distance from the surface. In these cases, a more economical approach than linear interpolation is to employ an exponential spacing function to cluster points near the body while keeping the overall number of points to a minimum. Elliptic smoothing of the algebraic grid was found to have negligible advantages in terms of solution quality.

After the initial grid has been defined, the outer iteration loop is begun to converge the flow solution. In this loop, the equivalent flow is first solved using a standard panel code implementation. For the first iteration, the airfoil shape and domain of the Laplacian flow is taken to be the same as that provided by the initial grid for the subsonic flow. Alternately, one could first distort the subsonic domain through a uniform stretching corresponding to an approximate Prandtl–Glauert-type correction. This approach was investigated, but no substantial reduction in the number of iterations required for convergence was noted. This result may be due to the inconsistencies in the tangency boundary conditions corresponding to the form of the Prandtl–Glauert rule that maps to an airfoil of the same chord corresponding to the $\bar{x}|_S = x|_S$ Dirichlet boundary conditions.

The choice of panel code used in this step is largely arbitrary, but certain concerns such as the ability to deal with finite thickness trailing edges must be considered. The panel code selected for this work is a formulation described by Moran [15] and based on some of the earliest implementations developed by Hess and Smith [17]. The formulation consists of a constant-strength source panel distribution that incorporates a single discrete vortex located at the quarter-chord location. The source distribution accounts for the airfoil thickness effects and provides excellent ability for dealing with thick trailing edges. The discrete vortex is used to satisfy the Kutta condition and to enforce the proper circulation for lifting cases. To provide the flow estimates needed for the coordinate mapping, the field solution must be calculated at all nodes in the grid and not just along the profile surface.

After calculating an estimate for the equivalent flow, the coordinate mapping is then solved. Because the mapping is an elliptic boundary value problem, it can be calculated with any of a variety of techniques developed for problems such as smoothing of structured grids or for steady subsonic compressible flow solutions. In this work, an iterative finite difference technique with successive line over-relaxation (SLOR) is adopted. Details of this method, including difference stencils and other equations, are presented in German [16], and we limit the discussion here to a prose overview of the numerical algorithm.

The first step in implementing the mapping method is to develop finite difference approximations of the Beltrami Eqs. (9) and (10). Second-order central difference approximations are employed for both the first and second coordinate derivatives within the domain interior, and second-order one-sided difference stencils are used at the boundaries. The estimates for the flow angle expression λ and the density ρ that appear in the Beltrami equations are set by transforming the panel code solution from the prior iteration to the original compressible coordinate frame using the covariant velocity transformation laws outlined in Eq. (15). The density is then determined from the velocity in the original frame through Eq. (2). The values λ and ρ serve as forcing functions that drive grid spacing in the mapping in a way analogous to control functions in Poisson-based elliptic grid smoothers.

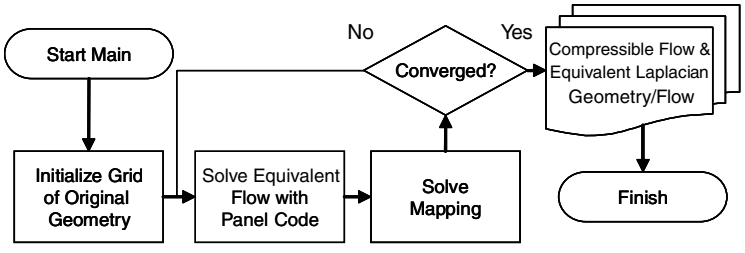

Fig. 2 Overall solution algorithm; outer loop.

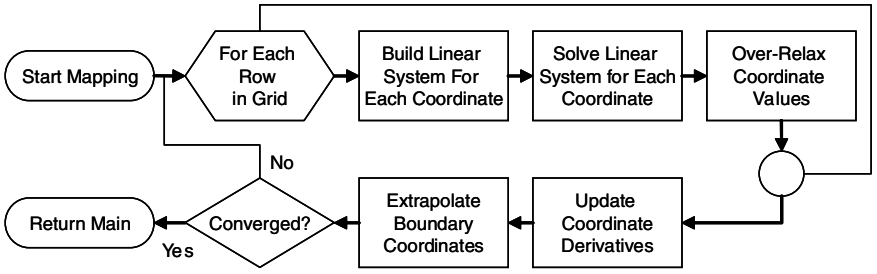

Fig. 3 Coordinate mapping solution algorithm; inner loop.

The finite difference stencils are then arranged into linear systems whose solutions are the $(\bar{x}, \bar{y})$ coordinate values along a particular grid row, and the SLOR method is implemented to solve the coordinates throughout the grid. SLOR and other iterative finite difference techniques are described in detail in Tannehill et al.[18]. To determine the coordinate solution, the SLOR algorithm shown in Fig. 3 is implemented. The algorithm sweeps through lines in the grid interior V solving the linear systems corresponding to each row of nodes. After each row has been solved, the calculated coordinate values are modified by an over-relaxation step, which produces a weighted average biased toward the current coordinate iterates relative to the prior iterates to accelerate convergence. Once the sweep through the interior grid rows is complete, the coordinate derivative expressions are updated based on the interior solution, and the grid boundaries are updated by extrapolation using the interior derivatives. The boundary conditions given in Eq. (13) require that the x coordinates remain the same along the inner and outer domain boundaries S_I and S_O, and so only the y coordinates are updated through extrapolation. On the cut boundaries B_+ and $B-$, the conditions matching the y coordinates given by Eq. (14) must be enforced, and so only the x coordinates are updated. Because of the interdependence of the coordinates on each row in the grid through the finite difference stencils, this process of sweeping through the grid must be iterated to convergence. The convergence criterion for this iteration is a sum-squared difference in coordinate values throughout the grid.

After the coordinate mapping is complete, the overall solution must also be checked for convergence because of the interdependence of the mapping and flow solutions. A variety of convergence tests could be devised, based either on flow parameters or on the coordinate mapping. In this implementation, we base the overall algorithm convergence on the coordinate mapping by specifying a change in the sum-squared difference of the grid points in the coordinates of the equivalent flow. This convergence criterion is identical to that used in the SLOR coordinate mapping itself, except, in this case, grids obtained in consecutive outer-loop iterations are compared instead of those in consecutive inner-loop iterations. If this convergence criterion for the overall algorithm is met, both the flow and the mapping solutions are considered complete; otherwise, a subsequent iteration of flow solution followed by coordinate mapping is performed. In performing this outer-loop iteration, over-relaxation could be employed to accelerate convergence, but this approach was not employed to produce the results presented in this paper.

Convergence histories for the algorithm for the $M_\infty = 0.375$ flow over a nonlifting circular cylinder corresponding to the results in Sec. IV.A are shown in Figs. 4 and 5. Figure 4 presents the outer-loop sum-squared residual convergence, and Fig. 5 shows the residual for the inner-loop coordinate mapping solution corresponding to the last outer-loop iteration. Both histories indicate log-linear convergence behavior after the first several iterations. These overall convergence trends can be noted in all solutions, but the rates of convergence appear to depend strongly on the magnitude of the freestream Mach number and somewhat on the profile thickness. Although the nested iterative structure of this algorithm is not as efficient as the direct approach of solving the compressible flow and then the equivalent flow mapping only once, wall time on a typical 2007-era personal computer is nonetheless only of the order of tens of seconds for a converged solution to the types of subsonic two-dimensional problems considered in this paper.

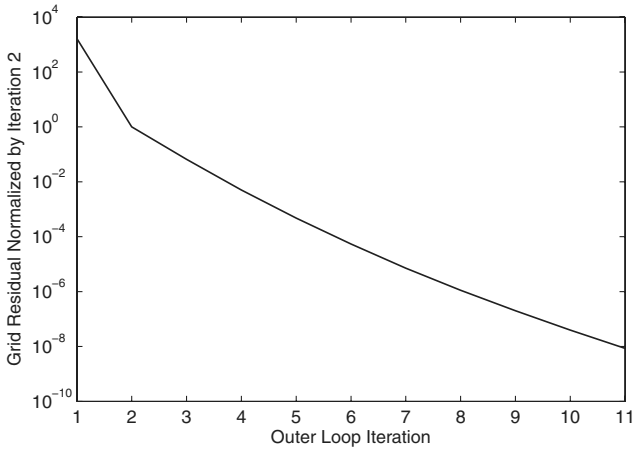

Fig. 4 Outer-loop residual for a nonlifting circular cylinder at $M_\infty = 0.375$.

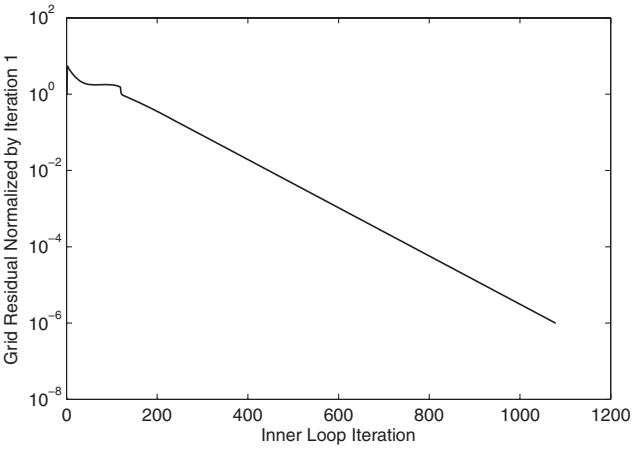

Fig. 5 Inner-loop residual for a nonlifting circular cylinder at $M_\infty = 0.375$ corresponding to the last outer-loop iteration.

IV. Results

A. Circle

This section presents the results for equivalent Laplacian flows over a circle. The flows are symmetric and nonlifting, and the Kutta condition is therefore not explicitly enforced in the flow solution algorithm.

We first discuss subsonic flow with a freestream Mach number of 0.375. The surface pressure coefficient distribution for this case is shown in Fig. 6 compared with Prandtl–Glauert and Kármán–Tsien corrections of the incompressible result as well as to the Rayleigh–Janzen expansion solution for the maximum velocity obtained by

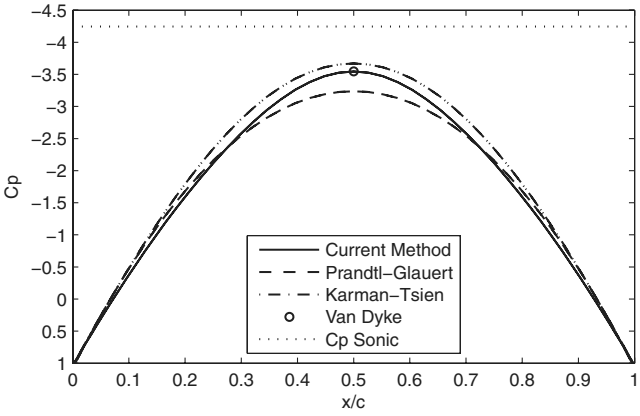

Fig. 6 Surface pressure coefficients for the circle.

Van Dyke [19]. Because of symmetry, this point of maximum velocity occurs at the maximum thickness point on the circle. Van Dyke's solution, which consists of 29 terms in a series of integer powers of M_∞^2, is given by

$$q_{\max} = q_\infty \sum_{n=1}^{29} q_n (M_\infty^2)^{n-1} \tag{29}$$

The coefficients q_n obtained by Van Dyke are presented in Table 1. As shown in Fig. 6, the solution from the present method matches the Van Dyke result and lies generally between the two compressibility corrections.

The original and distorted domains are shown superimposed in Fig. 7. The original domain is plotted relative to the (x, y) Cartesian coordinate axes, and the equivalent Laplacian domain is plotted relative to $(\bar{x}, \bar{y})$ axes treated as Cartesian coordinates. The results show that the body shape seen by the equivalent flow is oblonged and ellipselike, with its major axis oriented in the crossflow direction. Although the shape of the distorted body is generally reminiscent of an ellipse, Fig. 8 shows that the stretching of the equivalent Laplacian shape is more localized.

The increased thickness of the equivalent shape is necessary because the flow must be accelerated more through turning in the Laplacian flow in order to produce the same pressure changes as in a compressible flow with lesser turning. This behavior is fundamentally similar to the cross-stream stretching of an airfoil that results from the form of the Prandtl–Glauert rule that matches chord and pressure coefficients in the related airfoils [8].

Another notable feature of the distorted domain is the shape of the far-field boundary. Whereas the inner boundary is stretched to a greater thickness, the outer boundary is compacted. The far-field boundary condition was $\bar{x}|_{S_O} = x|_{S_O}$, and so the resulting shrinking is

Table 1 Terms in the Rayleigh–Janzen expansion for the circle of Van Dyke [19]

n	q_n	n	q_n
1	2.00000000000000	16	$4.26997505742413 \times 10^8$
2	1.166666666666667	17	$2.16247145908896 \times 10^9$
3	2.57833333333333	18	$1.10463770836747 \times 10^{10}$
4	7.51464814814814	19	$5.68649851009948 \times 10^{10}$
5	$2.55904074326026 \times 10^1$	20	$2.94779009123257 \times 10^{11}$
6	$9.62632913824853 \times 10^1$	21	$1.53777835504235 \times 10^{12}$
7	$3.87923452464374 \times 10^2$	22	$8.06853184029690 \times 10^{12}$
8	$1.64399333300068 \times 10^3$	23	$4.25587560801023 \times 10^{13}$
9	$7.23987123576189 \times 10^3$	24	$2.25576351728074 \times 10^{14}$
10	$3.28626654734814 \times 10^4$	25	1.2010117×10^{15}
11	$1.52864040612112 \times 10^5$	26	6.4210705×10^{15}
12	$7.25593930837266 \times 10^5$	27	3.446256×10^{16}
13	$3.50326365998740 \times 10^6$	28	1.856327×10^{17}
14	$1.71617906236987 \times 10^7$	29	1.00329×10^{18}
15	$8.51351821010245 \times 10^7$		

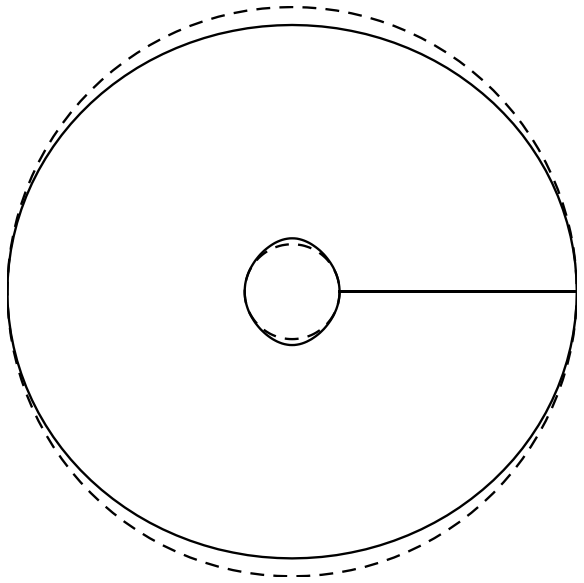

Fig. 7 Original (dashed) and equivalent Laplacian (solid) solution domains for the circle.

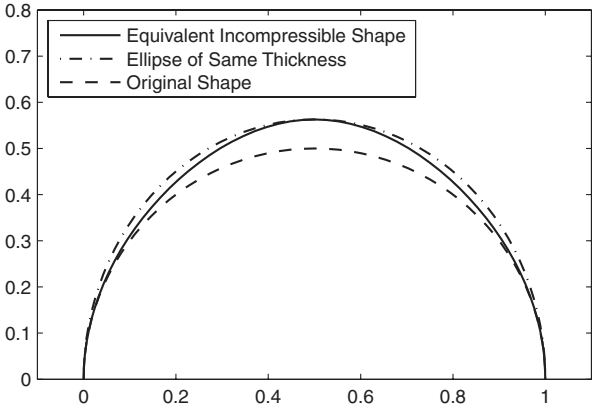

Fig. 8 Comparison of the equivalent Laplacian shape for the circle to an ellipse.

directly apparent in the y extent of the boundary. The local distortion effects at this boundary are negligible because the flow perturbations are vanishingly small in the far field. The result is therefore a nearly affine scaling of the boundary and its immediate neighborhood of the magnitude given by Eq. (19). Because the inner boundary is stretched and the outer boundary is compacted, this behavior is unlike the effects of the various forms of the Prandtl–Glauert and Göthert rules, which apply a uniform stretching or shrinking throughout the entire domain. That is, if the far field is stretched by the application of one of these classical methods, the airfoil is stretched by the same factor.

Another perspective of the distortion induced by the coordinate mapping is shown in Fig. 9. This figure depicts two views of the near-body domain. The first shows a net of coordinate curves of constant $\bar{x}$ and $\bar{y}$ on a plane with Cartesian axes x and y. The second shows the converse relationship with coordinate curves of constant x and y plotted on a plane with axes $\bar{x}$ and $\bar{y}$. Curves of constant x and y on the first plot would form a perfect Cartesian net, whereas the same result would be achieved for curves of constant $\bar{x}$ and $\bar{y}$ on the second plot.

The main behavior to be observed in these figures is the deviation of the coordinate curves from a perfectly square Cartesian net. The amount of deviation from this square net is indicative of the global and local strengths of the coordinate transformation. Large-scale global effects of the transformation tend to stretch the coordinate curves apart, generally mapping the squares uniformly into

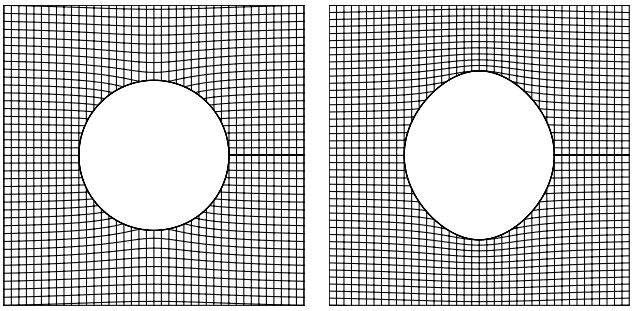

a) b)

Fig. 9 Mapping for the circle at $M_\infty = 0.375$ showing a) $(\bar{x}, \bar{y})$ coordinate curves in the (x, y) plane, and b) (x, y) coordinate curves in the $(\bar{x}, \bar{y})$ plane.

rectangles. The magnitude of these global effects is driven primarily by the freestream Mach number. Local effects resulting from high flow velocities near the body produce curvature in the coordinate curves.

For this case, global effects are barely visible because the freestream Mach number of 0.375 is too low. Although the global effects are weak, the local effects are quite strong, with significant curvature of the coordinate curves in the vicinity of the maximum velocity region.

The ability to capture these types of local effects is perhaps the greatest advantage of the method presented here compared with the Prandtl–Glauert- and Göthert-type transformations that are based on the freestream Mach number. Flows over thick bodies such as the circular cylinder cannot credibly be corrected for compressibility with these classical methods because the dominant flow effects are local and not global. Although the Kármán–Tsien method captures local effects to some extent, it is limited in accuracy because of its reliance on the tangent gas law.

Figure 10 shows the maximum velocity on the circle as a function of the freestream Mach number. In the incompressible limit, the peak velocity ratio is $V_{\max}/V_\infty = 2$. The value of this maximum increases with freestream Mach number, passing $V_{\max}/V_\infty = 2.327$ at the critical Mach number $M_\infty = 0.3982$. The results produced by the numerical method are compared with those found from Van Dyke's series expansion calculated using Eq. (29) and the series terms given in Table 1. Excellent agreement is obtained.

Among the most interesting aspects of Fig. 10 is that the results agree well even for the supercritical case at $M_\infty = 0.425$. Although the present method is expected to be invalid for supercritical Mach numbers, the result obtained by Van Dyke is not restricted to hold only in the subsonic regime. Indeed, his purpose in developing the high-order expansion for the circle was to attempt to answer the so-called transonic controversy of whether or not it is possible to maintain shock free flow about a fixed shape over a range of supercritical Mach numbers [19–21].

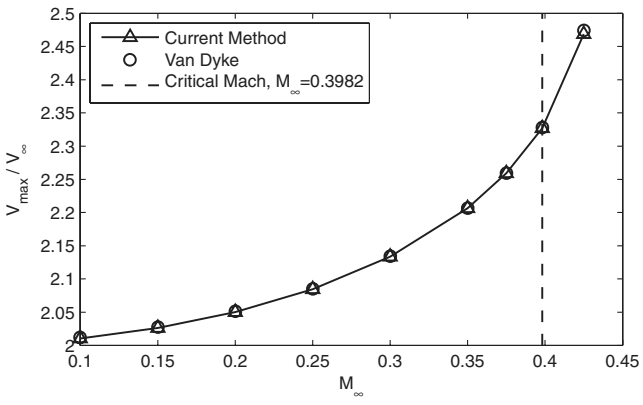

Fig. 10 Dependence of maximum velocity on freestream Mach number.

If Van Dyke's result is expected to hold above the critical Mach number and the method developed here is expected to be invalid in this regime, we are faced either with a contradiction or with a result at $M_\infty = 0.425$ that is obtained by happenstance. One possibility is that the size and magnitude of the supersonic region at $M_\infty = 0.425$ are small enough that the result obtained with the mapping method is nearly correct. If this is the case, the conclusion that the method is generally invalid in the supercritical region can be maintained. This viewpoint is supported by the fact that the error grows substantially from Van Dyke's result at this point (although it is still small), as indicated in Fig. 10. Evidence towards the validity of the method being limited to the subsonic range is also provided by the extreme difficulty with convergence obtained at even slightly higher supercritical Mach numbers.

Some of the equivalent shapes obtained for the sweep of freestream Mach numbers are shown in Fig. 11. As discussed in relation to the $M_\infty = 0.375$ case, the general effect of the coordinate transformation is to stretch the circle along the y axis into a shape somewhat similar to an ellipse. The magnitude of this cross-stream stretching is dependent on the Mach number, with higher Mach numbers lending to greater shape distortion.

B. NACA 0012 Profile

In this section, we examine solutions of equivalent Laplacian flow fields over the NACA 0012. First, we examine the results for flow at $M_\infty = 0.72$ and zero incidence. The surface pressure distributions for this case are shown in Figs. 12 and 13. Figure 12 compares the results for the subsonic flow to the accepted potential flow test results of Lock [22]. These subsonic results were obtained by transforming the Laplacian panel code solution to the frame of the subsonic flow.

Figure 13 shows the pressure distribution at the suction peak compared with those obtained by Prandtl–Glauert and Kármán–Tsien corrections of the incompressible flow over the original profile shape. The behavior depicted in this figure is characteristic of one of the weaknesses of the classical compressibility corrections. Because they act by a transformation of the pressure coefficients of the form $C_p|_x = f(C_{p,\text{incomp.}}|_x)$ that depends only on the local incompressible

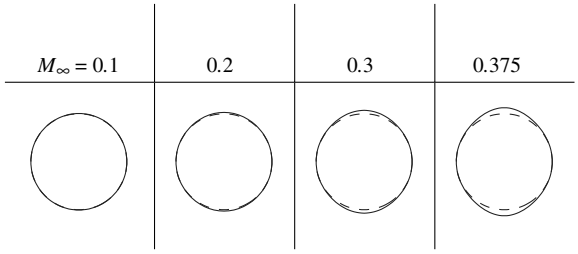

Fig. 11 Laplacian equivalent shapes to the circular cylinder.

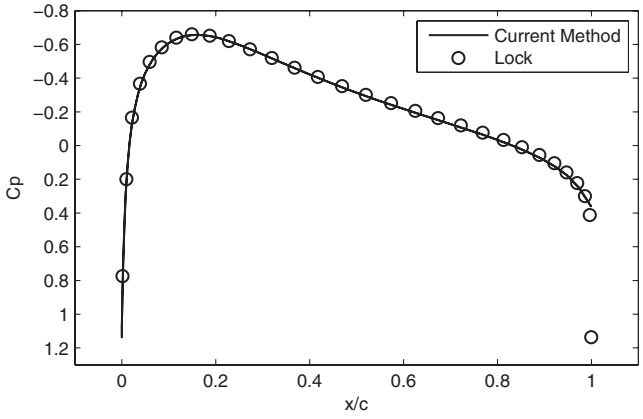

Fig. 12 Surface pressure coefficients for the NACA 0012, $M_\infty = 0.72$, $\alpha = 0$ deg.

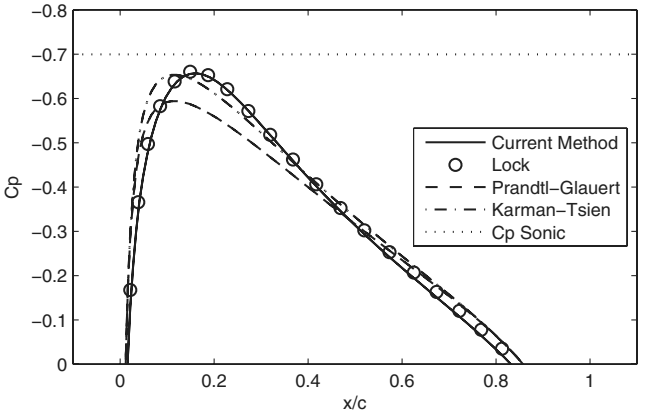

Fig. 13 Surface pressure coefficients for the NACA 0012, $M_\infty = 0.72$, $\alpha = 0$ deg, with suction peak detail.

value, they do not capture compressibility effects that might be considered "integral" in nature, that is, that depend on information not available locally in the incompressible flow solution). The shifting of the suction peak aftward along the airfoil is an example of this type of integral effect that is illustrated in Fig. 13. Whereas the Prandtl–Glauert and Kármán–Tsien methods primarily scale the local incompressible C_p values and, therefore, miss the shift in x/c of the peak, the numerical method developed in this work captures the shift correctly because the nonlocal information is propagated appropriately in the coordinate mapping.

We now discuss the coordinate mapping itself. Figure 14 shows the boundaries of the equivalent Laplacian domain superimposed over the original domain corresponding to the compressible flow. As with the circle, the inner boundary of the equivalent domain is thickened while the outer boundary is compacted. The overall magnitude of the distortion is greater for this case than for the circle because of the higher freestream Mach number. This greater distortion is particularly evident in the movement of the outer boundary, which is much more significant here than for the circle.

The graphic on the left in Fig. 15 shows coordinate curves of constant coordinates $\bar{x}$ and $\bar{y}$ of the equivalent flow plotted on a plane defined by Cartesian axes x and y of the given subsonic flow. The graphic on the right shows coordinate curves of constant x and y plotted on a plane defined by Cartesian axes $\bar{x}$ and $\bar{y}$. As discussed in relation to the circle, the primary features to examine in these plots are the uniform spacing and the curvature of these coordinate lines. A

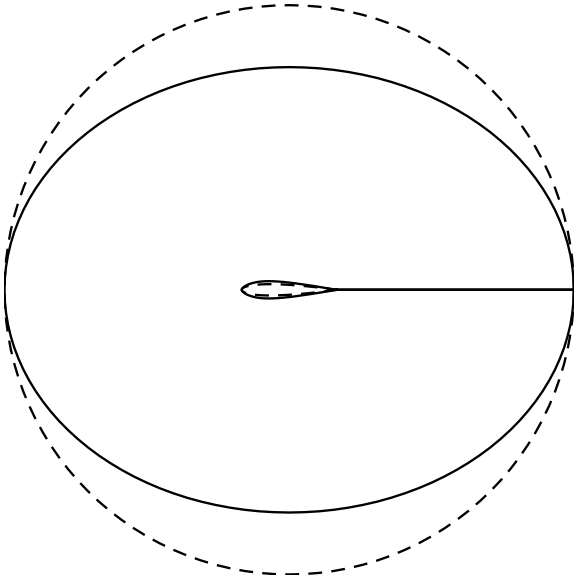

Fig. 14 Original (dashed) and Laplacian equivalent (solid) solution domains for the NACA 0012, $M_\infty = 0.72$, $\alpha = 0$ deg.

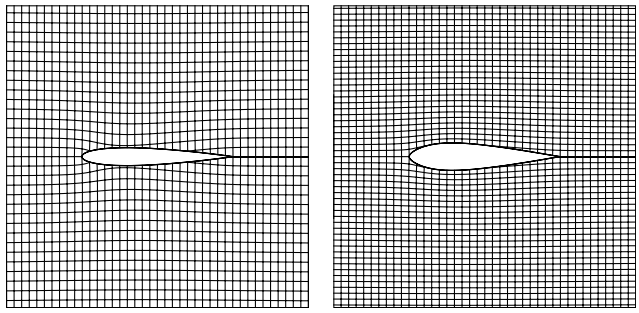

a) b)

Fig. 15 Mapping for the for the NACA 0012, $M_\infty = 0.72$, $\alpha = 0$ deg showing a) $(\bar{x}, \bar{y})$ coordinate curves in the (x, y) plane, and b) (x, y) coordinate curves in the $(\bar{x}, \bar{y})$ plane.

uniform spacing between the lines that produces rectangular cells from the nominally square net is indicative of the global effect of freestream Mach number. Curvature in the lines is indicative of local flow accelerations. Compared with the circle, these results show a greater uniform distortion as evidence by the generally rectangularly shaped cells, with the long axis along y in the left plot and the long axis along $\bar{x}$ in the right plot. This increased distortion is due to the greater Mach number for this case compared with that of the circle. The regions of greatest curvature of the coordinate lines are near the leading edge and near the suction peak where velocity magnitudes are most different from their freestream values.

Next, we examine the results for the flow over the NACA 0012 at $M_\infty = 0.63$ and an angle of attack of $\alpha = 2$ deg. In these simulations, the Kutta condition is enforced, so that the flows are not only asymmetric but also circulatory.

The surface pressure distribution is presented in Figs. 16 and 17. In Fig. 16, the results are compared with the solutions developed by Lock [22]. Figure 17 shows a magnified depiction of the solution near the suction peak along with Prandtl–Glauert and Kármán–Tsien corrections of the incompressible flow over the original airfoil. Similar to the symmetric solution, the Prandtl–Glauert result underpredicts the peak, whereas the Kármán–Tsien method overpredicts. The inability of the corrections to capture the integral compressibility effect of the aft shift of the suction peak is also evident in this case.

The overall domain distortion is qualitatively similar to that for the case of symmetric flow at $M_\infty = 0.72$ shown in Fig. 14, as the effects of slight nonzero incidence and circulation are not prominent in the large scale of the entire domain. That is, the global domain shape for the relatively thin body of the NACA 0012 is affected primarily by the freestream Mach number and not small angles of attack. The effect of angle of attack and circulation can be seen, however, in the magnified view of the airfoil shape and coordinate lines in the leading-edge region shown in Fig. 18. The dominant effect of angle

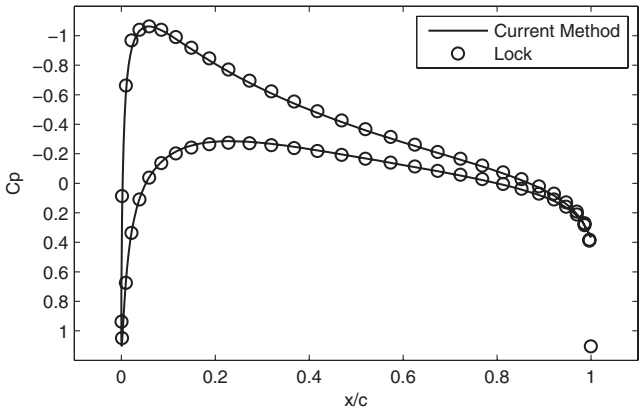

Fig. 16 Surface pressure coefficients for the NACA 0012, $M_\infty = 0.63$, $\alpha = 2$ deg.

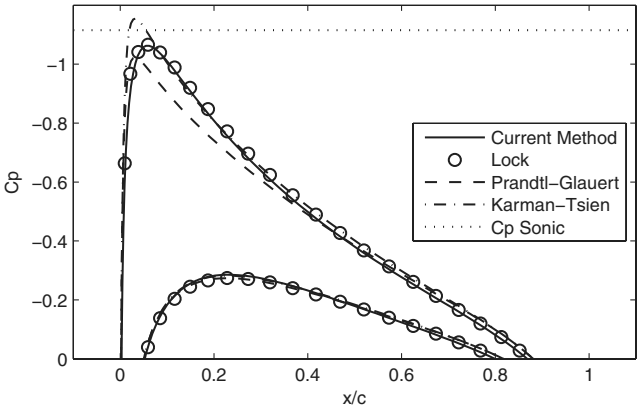

Fig. 17 Surface pressure coefficients for the NACA 0012, $M_\infty = 0.63$, $\alpha = 2$ deg, with suction peak detail.

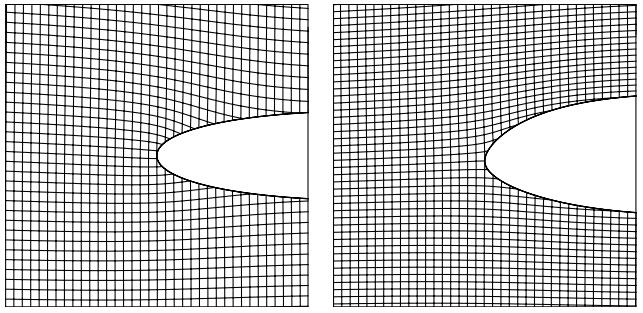

a) **b)**

Fig. 18 Mapping for the for the NACA 0012, $M_\infty = 0.63$, $\alpha = 2$ deg showing a) $(\bar{x}, \bar{y})$ coordinate curves in the (x, y) plane, and b) (x, y) coordinate curves in the $(\bar{x}, \bar{y})$ plane, with leading-edge detail.

of attack on the transformation is to cause a localized leading-edge droop relative to the original airfoil, producing a slight amount of positive camber in the immediate forebody region. The effect also has the appearance of thickening the entire leading-edge region slightly. The asymmetric local curvature of the coordinate lines in the stagnation and maximum velocity regions is also visible in this figure.

An interesting question with regards to this asymmetrical case with circulation is how the coordinate mapping affects the stagnation streamline of the equivalent flow. The effect, shown in Figs. 19 and 20, is to rotate the leading-edge stagnation point downward in correspondence with the leading-edge droop. The stagnation streamline therefore deviates downward from the compressible flow streamline as we move forward of the body. The deviation is significant and noticeable at a distance of two chord lengths upstream of the airfoil as shown in Fig. 19. Although the leading-edge stagnation streamline is significantly altered, the trailing-edge streamline remains largely indistinguishable from that of the compressible flow and is therefore not plotted. This result occurs because the minor influence of angle of attack in this region produces vanishing asymmetry in the equivalent airfoil in the trailing-edge region. Because the Kutta condition is enforced crisply for both the compressible and equivalent Laplacian flows, the trailing-edge stagnation streamlines for both flows proceed smoothly along the bisection ray from the finite-thickness trailing edge and are for all practical purposes coincident.

The previous results presented for the NACA 0012 were intended to provide validating comparisons of the method to known results in the literature and to provide general insights into the phenomena associated with the transformed shapes and coordinate systems of typical equivalent Laplacian flows. Although insightful, these point solutions do not give an adequate depiction of how equivalent shapes change as a function of the flow parameters. To develop such an understanding, we now perform a systematic variation of the angle of attack and freestream Mach number and tabulate the equivalent shapes obtained.

The study conducted consists of solving a two-dimensional matrix of flow solutions corresponding to Mach numbers ranging from 0.3 to 0.7 in increments of 0.1 and to angles of attack ranging from 0 to 8 deg in 2 deg increments. The full grid of solutions was not completed because we must limit our results only to subcritical cases. Estimates of the locations of the critical conditions in this matrix were made, and the resulting solutions were then checked to verify that they satisfied the subcritical criterion. To examine the most extreme conditions possible, care was taken to consider cases as close to the critical conditions as feasible.

The primary effects of the transformation on the profile shape are a thickening with increasing Mach number and an increase in leading-edge camber with angle of attack. These effects can be seen in Fig. 21, which presents a magnified view of the airfoil forebody region for the matrix of Mach numbers and incidence angles. The increased leading-edge droop with angle of attack is visible, particularly for the cases at intermediate M_∞ and α. Because lesser droop is visible for the lower Mach but higher angle cases, it appears that the magnitude of the leading-edge movement is more dramatically affected by Mach number than angle of attack.

The trends shown in this matrix of shapes are presented in a more quantitative fashion in Figs. 22 and 23. Figure 22 depicts the maximum thickness of the equivalent profiles as a function of Mach number and angle of attack. It is clear that the driving influence on thickness is primarily Mach number and not incidence, with incidence having an appreciable additional effect only at higher Mach numbers. The effect of the classical Prandtl–Glauert stretching factor of $1/\sqrt{1 - M_\infty^2}$ on the NACA 0012 profile is also plotted in the figure. Interestingly, the transformation developed in this work produces a smaller thickening at lower Mach numbers than the Prandtl–Glauert result and a larger thickening at higher Mach numbers. An additional and very intriguing result is that the x/c location of the maximum thickness $t_{\max}$ corresponds in both the original flow and the equivalent flow. That is, $(\bar{x}/c)|_{t_{\max}} = (x/c)|_{t_{\max}}$.

The behavior of the leading-edge droop with M_∞ and α is shown in Fig. 23. The trends are surprisingly regular, with nearly linear relationships between the displacement and angle of attack for all of the examined Mach numbers.

Fig. 19 Shift in the stagnation streamline from the original domain (dashed) to the equivalent incompressible domain (solid).

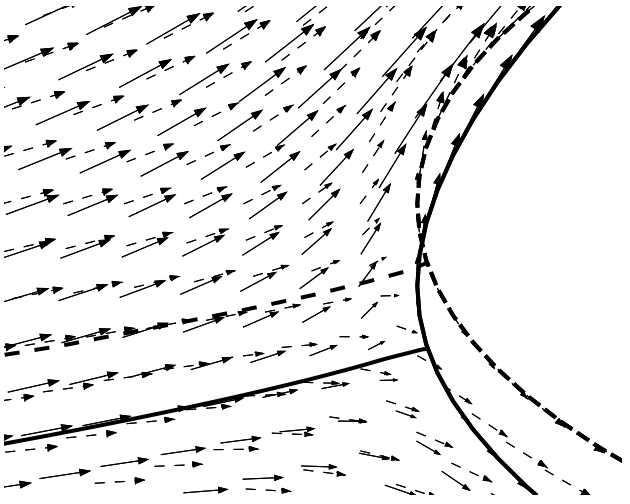

Fig. 20 Shift in the stagnation streamline from the original domain (dashed) to the Laplacian equivalent domain (solid), with leading-edge detail.

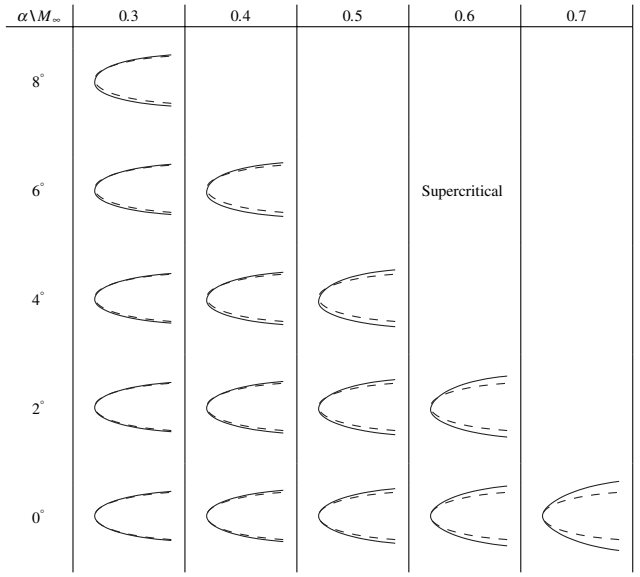

Fig. 21 Equivalent Laplacian airfoils to the NACA 0012, with leading-edge detail.

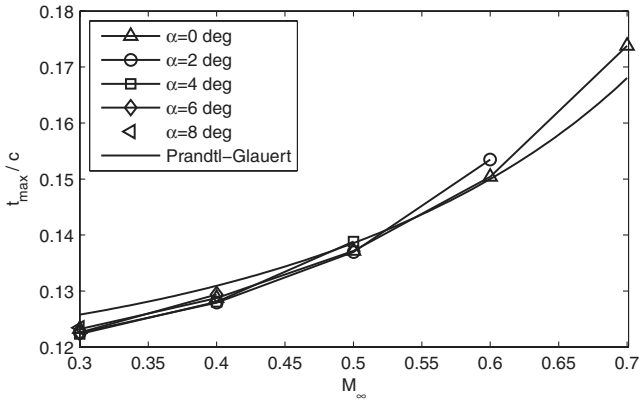

Fig. 22 Thickness of Laplacian equivalent airfoils to the NACA 0012.

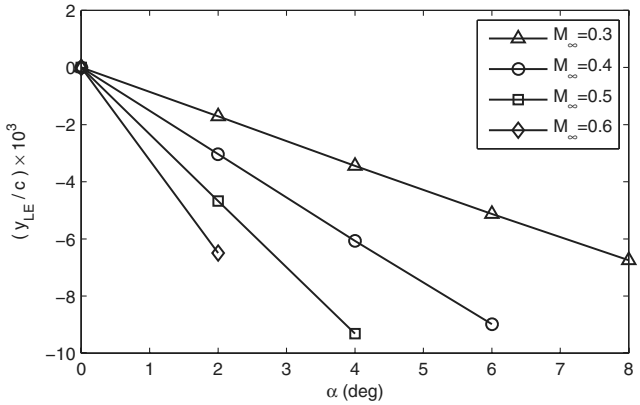

Fig. 23 Leading-edge droop of Laplacian equivalent airfoils to the NACA 0012.

V. Conclusions

A mapping approach for the solution of Laplacian flows equivalent to given subsonic compressible potential flows has been developed. The method is exact up to numerical precision for the steady nonlinear circulatory potential motion of fluids with arbitrary density–velocity relations. The approach employs a quasi-conformal transformation that depends on the density ρ and the flow angle expression λ of the compressible flow and forms elliptic partial differential equations for each coordinate. In this implementation, the coordinate boundary value problem is posed by specifying Dirichlet conditions on the abscissa coordinate $\bar{x}$ and conditions matching the $\bar{y}$ values along the two sides of the domain cut boundary. The far-field conditions on the flow indicate that the tangent of the angle of attack in the incompressible flow is larger than that of the compressible flow by the factor $1/\sqrt{1-M_\infty^2}$, which is the scaling factor of the Prandtl–Glauert approach for linear flows. Because the method is based on a pure coordinate transformation, scalar functions of the flow are invariant between the two domains, and the velocity transforms as a covariant vector. In particular, the density ρ varies from point to point in the equivalent Laplacian flow. This result indicates that the equivalent flow is kinematically identical to an incompressible flow in that the density does not appear in the continuity equation; however, it is not truly incompressible in the traditional sense.

Laplacian equivalents can be developed using this theory in at least two ways. The first is through a direct approach in which known subsonic compressible flow properties are provided as inputs to a numerical method for solving the mapping. The second approach is an indirect method in which an unknown subsonic flow is solved simultaneously with its Laplacian equivalent. With the latter approach, the equivalent flow may be solved with a standard boundary element method. This indirect technique is pursued in this work as a mechanism for validating the mapping approach. To accomplish this validation, subsonic flows are solved via their equivalents using a panel method that is valid only for Laplacian flows, and the resulting solutions are compared with known results in the literature.

Laplacian equivalents were developed for symmetric flows over a circle and both symmetric and lifting flows over a NACA 0012 profile. The resulting subsonic solutions for the circle were compared with the Rayleigh–Janzen expansion of Van Dyke [19] for the maximum velocity and showed good agreement. The mapping acted to thicken the circle into an ellipselike shape with the major axis oriented in the crossflow direction and to compact the far-field boundary in the y direction. These trends became more pronounced and localized near the suction peak as the freestream Mach number was increased toward the critical value of 0.3982.

The method was validated for the NACA 0012 by the favorable comparison of the subsonic potential solutions with those of Lock [22] at the conditions $M_\infty = 0.72$, $\alpha = 0$ deg and $M_\infty = 0.63$, $\alpha = 2$ deg. For the symmetric case, the mapping results were qualitatively similar to those of the circle with a thickening of the profile shape and the cross-stream shrinking of the far-field boundary. The $M_\infty = 0.63$, $\alpha = 2$ deg case was both asymmetric and circulatory through the enforcement of the Kutta condition. This case indicated an additional effect of the mapping, namely the introduction of leading-edge camber to the profile. The variation of the mapping effects with flow parameters was investigated by solving a matrix of subcritical M_∞ and α conditions. This investigation showed that the profile thickens with an increased freestream Mach number at a similar rate as the Prandtl–Glauert method, and more interestingly, it showed that the amount of leading-edge droop increases linearly with angle of attack across the range of Mach numbers.

The mapping method may find several useful theoretical and practical applications. The first possibility is in certain aerodynamic test scenarios. Because the mapping takes the subsonic flow over a closed profile to a second flow over a closed profile with the same tangency boundary conditions, the Laplacian equivalent has the kinematics of a physically obtainable real-world flow that could be demonstrated in an experimental setting. This capability could enable higher Mach subsonic flows to be emulated by testing the equivalent Laplacian geometry at a lower Mach number in a less costly facility. The effect would be to remove the influence of compressibility from the potential field, allowing viscous features of the flows to be examined in the equivalent flow and extrapolated to the subsonic geometry and conditions of interest. A difficulty to this

approach, however, is that each flow condition that must be examined requires its own airfoil test hardware and unique domain mapping. Perhaps the greater utility of the method, however, is to provide further insights into the nature of compressibility itself through understanding of the domain distortions of a Laplacian flow required to emulate the compressibility effects in the given subsonic flow.

Appendix

A partial differential equation of the form

$$A\frac{\partial^2\bar{y}}{\partial x^2}+B\frac{\partial^2\bar{y}}{\partial x\partial y}+C\frac{\partial^2\bar{y}}{\partial y^2}+D\frac{\partial\bar{y}}{\partial x}+E\frac{\partial\bar{y}}{\partial y}+F\bar{y}=G \tag{A1}$$

is classified based on the value of the quantity B^2-4AC, which is known as the discriminant. The equation is hyperbolic if the discriminant is positive, parabolic if the discriminant equals zero, and elliptic if the discriminant is negative [23]. Expanding Eq. (11) by the chain rule gives

$$\begin{aligned}&\left[\frac{(\rho/\rho_0)+(\rho_0/\rho)\lambda^2}{1+\lambda^2}\right]\frac{\partial^2\bar{y}}{\partial x^2}+2\lambda\left[\frac{(\rho/\rho_0)-(\rho_0/\rho)}{1+\lambda^2}\right]\frac{\partial^2\bar{y}}{\partial x\partial y}\\&+\left[\frac{(\rho/\rho_0)\lambda^2+(\rho_0/\rho)}{1+\lambda^2}\right]\frac{\partial^2\bar{y}}{\partial y^2}+\frac{\partial}{\partial x}\left\{\left[\frac{(\rho/\rho_0)+(\rho_0/\rho)\lambda^2}{1+\lambda^2}\right]\right\}\frac{\partial\bar{y}}{\partial x}\\&+\frac{\partial}{\partial x}\left\{\lambda\left[\frac{(\rho/\rho_0)-(\rho_0/\rho)}{1+\lambda^2}\right]\right\}\frac{\partial\bar{y}}{\partial y}+\frac{\partial}{\partial y}\left\{\lambda\left[\frac{(\rho/\rho_0)-(\rho_0/\rho)}{1+\lambda^2}\right]\right\}\frac{\partial\bar{y}}{\partial x}\\&+\frac{\partial}{\partial y}\left\{\left[\frac{(\rho/\rho_0)\lambda^2+(\rho_0/\rho)}{1+\lambda^2}\right]\right\}\frac{\partial\bar{y}}{\partial y}=0\end{aligned} \tag{A2}$$

Equation (A2) can be organized into the form of Eq. (A1) through the identification

$$\begin{aligned}A&=\left[\frac{(\rho/\rho_0)+(\rho_0/\rho)\lambda^2}{1+\lambda^2}\right]\\B&=2\lambda\left[\frac{(\rho/\rho_0)-(\rho_0/\rho)}{1+\lambda^2}\right]\\C&=\left[\frac{(\rho/\rho_0)\lambda^2+(\rho_0/\rho)}{1+\lambda^2}\right]\\D&=\frac{\partial}{\partial x}\left\{\left[\frac{(\rho/\rho_0)+(\rho_0/\rho)\lambda^2}{1+\lambda^2}\right]\right\}+\frac{\partial}{\partial y}\left\{\lambda\left[\frac{(\rho/\rho_0)-(\rho_0/\rho)}{1+\lambda^2}\right]\right\}\\E&=\frac{\partial}{\partial x}\left\{\lambda\left[\frac{(\rho/\rho_0)-(\rho_0/\rho)}{1+\lambda^2}\right]+\frac{\partial}{\partial y}\left\{\left[\frac{(\rho/\rho_0)\lambda^2+(\rho_0/\rho)}{1+\lambda^2}\right]\right\}\right\}\\F&=G=0\end{aligned} \tag{A3}$$

Forming and simplifying the discriminant gives

$$B^2-4AC=-4 \tag{A4}$$

Because the discriminant is a negative constant, the mapping is always elliptic in character. Elliptic equations require the specification of boundary conditions along all boundary curves of the two-dimensional domain.

Because the discriminant is independent of the flow solution, it may appear that the elliptic mapping described in this article could be used to transform all potential flows including those with sonic and supersonic regions to the canonical Laplacian form of incompressible flow. This must not be true, however, because of the general result in the theory of partial differential equations that states that a transformation between systems of real coordinates cannot change the type of a differential equation [24]. That is, sonic (parabolic) and supersonic (hyperbolic) regions cannot be mapped to an incompressible (elliptic) flow through this type of transformation.

Acknowledgments

The author would like to acknowledge the kind support of Dimitri Mavris of the Georgia Institute of Technology as this work was carried out. I am also indebted to Rob McDonald, now of California Polytechnic State University, San Luis Obsipo, for his valuable suggestions.

References

[1] Prandtl, L., "Ueber Strömungen Deren Geschwindigkeiten mit der Schallgeschwindigkeit Vergliecher Sind," *Journal of the Aeronautical Research Institute*, No. 65, 1930, p. 14.

[2] Prandtl, L., "General Considerations on the Flow of Compressible Fluids," NACA Technical Memorandum 805, 1936.

[3] Glauert, H., "The Effect of Compressibility on the Lift of an Aerofoil," *Proceedings of the Royal Society of London A*, Vol. 118, 1928, pp. 113–119.
doi:10.1098/rspa.1928.0039

[4] Göthert, B., "Plane and Three-Dimensional Flow at High Subsonic Speeds," NACA Technical Memorandum 1105, 1946.

[5] Chaplygin, S. A., "On Gas Jets," *Scientific Memoirs*, Vol. 21, 1904, pp. 1–121.

[6] Chaplygin, S. A., "On Gas Jets," NACA Technical Memorandum 1063, 1944.

[7] Tsien, H.-S., "Two-Dimensional Subsonic Flow of Compressible Fluids," *Journal of the Aeronautical Sciences*, Vol. 6, No. 10, 1939, pp. 399–407.

[8] Shapiro, A. H., *The Dynamics and Thermodynamics of Compressible Fluid Flow*, Ronald, New York, 1953.

[9] Bers, L., "On a Method of Constructing Two-Dimensional Subsonic Flows Around Closed Profiles," NACA Technical Note 969, 1945.

[10] Bers, L., "Velocity Distribution on Wing Sections of Arbitrary Shape in Compressible Potential Flow. I. Symmetric Flows Obeying the Simplified Density–Speed Relation," NACA Technical Note 1006, 1946.

[11] Bers, L., "Velocity Distribution on Wing Sections of Arbitrary Shape in Compressible Potential Flow. II. Subsonic Symmetric Adiabatic Flows," NACA Technical Note 1012, 1946.

[12] Bers, L., "Partial Differential Equations and Generalized Analytic Functions," *Proceedings of the National Academy of Sciences of the United States of America*, Vol. 36, No. 2, 1950, pp. 130–136.
doi:10.1073/pnas.36.2.130

[13] Lin, C. C., "On an Extension of the von Kármán–Tsien Method to Two-Dimensional Subsonic Flows with Circulation Around Closed Profiles," *Quarterly of Applied Mathematics*, Vol. 4, No. 3, 1946, p. 291.

[14] Lin, C. C., and Shen, S. F., "Studies of von Kármán's Similarity Theory and its Extension to Compressible Flows," NACA Technical Note 2541, 1951.

[15] Moran, J., *An Introduction to Theoretical and Computational Aerodynamics*, Wiley, New York, 1984.

[16] German, B. J., "A Riemannian Geometric Mapping Technique for Generating Incompressible Equivalents to Subsonic Potential Flows," Ph.D. Dissertation, Georgia Institute of Technology, Atlanta, GA, 2007.

[17] Hess, J. L., and Smith, A. M. O., "Calculation of Potential Flow About Arbitrary Bodies," *Progress in Aeronautical Sciences*, Pergamon, New York, Vol. 8, 1967, pp. 1–138.

[18] Tannehill, J. C., Anderson, D. A., and Pletcher, R. H., *Computational Fluid Mechanics and Heat Transfer*, Taylor and Francis, London, 1997.

[19] Van Dyke, M., "Long Series in Mechanics: Janzen–Rayleigh Expansion for a Circle," *Meccanica*, Vol. 33, No. 5, 1998, pp. 517–522.
doi:10.1023/A:1004324711194

[20] Van Dyke, M. D., and Guttmann, A. J., "Computer Extension of the M^2 Expansion for a Circle," *Bulletin of the American Physical Society*, Vol. 23, 1978, p. 996.

[21] Van Dyke, M. D., and Guttmann, A. J., "Subsonic Potential Flow Past a Circle and the Transonic Controversy," *Journal of the Australian Mathematical Society, Series B*, Vol. 2, 1983, pp. 243–261.

[22] Lock, R. C., "Test Cases for Numerical Methods in Two-Dimensional Transonic Flows," AGARD Rept. 575, 1970.

[23] Farlow, S. J., *Partial Differential Equations for Scientists and Engineers*, Dover, New York, 1993.

[24] Garabedian, P. R., *Partial Differential Equations*, American Mathematical Society, Providence, RI, 1998.

A. Plotkin
Associate Editor